Monthly Notices of the ROYAL ASTRONOMICAL SOCIETY

MNRAS **527,** 7825–7834 (2024) https://doi.org/10.1093/mnras/stad3695
Advance Access publication 2023 November 28

Narrow absorption line outflow in Seyfert 1 galaxy J1429+4518: outflow's distance from the central source and its energetics

M. Dehghanian ,★ N. Arav , D. Byun , G. Walker and M. Sharma
Department of Physics, Virginia Tech, Blacksburg, VA 24061, USA

Accepted 2023 November 27. Received 2023 October 16; in original form 2023 August 25

ABSTRACT

In the *Hubble Space Telescope*/Cosmic Origins Spectrograph spectrum of the Seyfert 1 galaxy 2MASX J14292507+4518318, we have identified a narrow absorption line outflow system with a velocity of -151 km s^{-1}. This outflow exhibits absorption troughs from the resonance states of ions like C IV, N V, S IV, and Si II, as well as excited states from C II* and Si II*. Our investigation of the outflow involved measuring ionic column densities and conducting photoionization analysis. These allow the total column density of the outflow to be estimated as $\log N_{\rm H} = 19.84$ cm^{-2}, its ionization parameter to be $\log U_{\rm H} = -2.0$, and its electron number density to be $\log n_{\rm e} = 2.75$ cm^{-3}. These measurements enabled us to determine the mass-loss rate and the kinetic luminosity of the outflow system to be $\dot{M} = 0.22$ M$_\odot$ yr^{-1} and $\log \dot{E}_{\rm K} = 39.3$ erg s^{-1}, respectively. We have also measured the location of the outflow system to be at ∼275 pc from the central source. This outflow does not contribute to the active galactic nucleus (AGN) feedback processes due to the low ratio of the outflow's kinetic luminosity to the AGN's Eddington luminosity ($\dot{E}_{\rm K}/L_{\rm Edd} \approx 0.00025$ per cent). This outflow is remarkably similar to the two bipolar lobe outflows observed in the Milky Way by *XMM–Newton* and *Chandra*.

Key words: galaxies: active – galaxies: individual: 2MASX J14292507+4518318 – quasars: absorption lines – galaxies: Seyfert.

1 INTRODUCTION

Absorption outflows from active galactic nuclei (AGNs) are frequently suggested as potential contributors to the AGN feedback processes. Various studies have discussed this idea, e.g. Silk & Rees (1998), Scannapieco & Oh (2004), Yuan et al. (2018), Vayner et al. (2021), and He et al. (2022). Absorption lines found in the rest-frame ultraviolet (UV) spectra are typically grouped into three main categories based on their characteristics: broad absorption lines (BALs) that have a width of ≥2000 km s^{-1}, narrow absorption lines (NALs) with a width of ≤500 km s^{-1}, and a middle subgroup known as mini-BALs (Itoh et al. 2020). When it comes to BALs, it is clear that the absorbing gas is connected to the AGN (Vestergaard 2003) and could indeed have a noticeable impact on suppressing the star formation rate within the host galaxies (Chen et al. 2022); however, the nature of NAL outflows is less understood. This is due to the challenge of discerning intrinsic NALs (associated NALs) from those NALs that are unrelated to the quasars (intervening NALs). Intervening NALs can originate from various sources, including intervening galaxies, intergalactic clouds, Milky Way gas, or gas within the host galaxies of the quasars (Misawa et al. 2007a). Several studies (e.g. Misawa et al. 2007a; Chen & Qin 2013; Chen et al. 2018b, 2020) have highlighted the point that variations in the absorption lines serve as a robust indicator to distinguish between NALs arising from the outflow system, or those called intervening NALs. These variations in absorption lines typically arise from changes in the column density of absorbing gas as part of the intrinsic mechanism.

Shen & Ménard (2012) and Chen et al. (2018a) explain that a velocity of 3000 km s^{-1} is often used to limit associated NALs; however, it should also be noted that some NAL outflows with velocity being obviously larger than 3000 km s^{-1} have been observed (Hamann et al. 2011; Chen & Qin 2013). Using large samples of the Sloan Digital Sky Survey (SDSS) quasar C IV and Mg II NALs, Chen & Pan (2017) discuss that the velocity boundary is associated with the quasar luminosity. In the study referred to, it is proposed that velocity thresholds of 4000 km s^{-1} be used to identify quasar C IV-associated NALs and velocity thresholds of 2000 km s^{-1} be employed to identify quasar Mg II-associated NALs.

Despite the fact that NALs have received less attention than BALs, they hold great potential as a useful tool for investigating the physical properties of outflows because of these two significant reasons (Misawa et al. 2007b):

(i) NALs do not have the problem of self-blending, which is defined as blending blue and red components of doublets like C IV λλ1548, 1551;
(ii) NALs appear in a larger variety of AGNs, whereas BALs are mostly detected in radio-quiet quasars.

This paper identifies and analyses the NAL outflow system of the AGN 2MASX J14292507+4518318 (hereafter J1429+4518) using the observations performed by the *Hubble Space Telescope* (*HST*) in 2021. For this object, the intrinsic nature of the NAL is deduced from the presence of several excited state absorption narrow lines observed in the spectrum. The paper's structure is as follows.

In the next section, we describe the observations and data acquisition of the target. It is followed by Section 3, which includes the

★ E-mail: dehghanian@vt.edu

analysis and explains the methods used in the paper. Section 3 also details the approaches used to calculate the ionic column densities of the NALs. Calculations of the electron number density and location of the outflow, along with the best photoionization solution, are all included in Section 3. Part of Section 3 is dedicated to finding the central source's mass and the AGN's Eddington luminosity. These calculations are followed by estimating the energetics of the outflow system. Section 4 discusses the stability of the outflow and indicates the importance of the NALs in general. In this section, we also compare our NAL outflow system with two lobe outflows detected in the Milky Way. Finally, Section 5 gives a summary of what we have done here and concludes the paper.

Here we adopted a cosmology with $h = 0.696$, $\Omega = 0.286$, and $\Omega_v = 0.714$ (Bennett et al. 2014). We used the PYTHON astronomy package ASTROPY (Astropy Collaboration 2013, 2018) for our cosmological calculations, as well as SCIPY (Virtanen et al. 2020), NUMPY (Harris et al. 2020), and PANDAS (Reback et al. 2021) for most of our numerical computations. For our plotting purposes, we used MATPLOTLIB (Hunter 2007).

2 OBSERVATIONS

J1429+4518 is a Seyfert 1 galaxy, located at redshift $z = 0.07454$, with J2000 coordinates at RA = 14:29:25.07 and Dec. = +45:18:31.93. The galaxy was observed using the *HST* Cosmic Origins Spectrograph (*HST*/COS) on three separate occasions, 2021 September 19, 2021 December 20, and 2021 December 21, as part of *HST* Proposal 16301 (Putman et al. 2020). The first observation utilized the G130M grating, while the subsequent two observations used G160. For this study, we excluded the observation taken on 2021 December 21, as it covered the same wavelength range as the other December observation but had a shorter exposure time. The spectral data for both observations are displayed in Figs 1 and 2.

After obtaining the relevant data from the *Mikulski Archive for Space Telescopes* (*MAST*), we detected an outflow at a velocity of $v = -151$ km s^{-1}, with blueshifted ionic absorption lines denoted by red vertical lines in Figs 1 and 2. Among the identified absorption lines, several well-known resonance doublets, such as C IV and N V, were observed. Additionally, we identified absorption lines arising from excited states, such as C II* and Si II*.

2.1 Redshift considerations

The redshift assigned to the object ($z = 0.07454$) is the sole value documented in the SIMBAD Astronomical Database[1] and is derived from optical data analysis. Despite the NASA/IPAC Extragalactic Database (NED)[2] reporting seven different redshift values (within the range of $z = 0.0745$ to $z = 0.0748$) for this object, their preferred redshift in their data bases is also documented as 0.07454. Furthermore, the SDSS Science Archive Server (SAS)[3] confirms this redshift for the same object. In the interest of maintaining consistency with these data bases, we have adopted the same redshift value. It is essential to acknowledge the inherent uncertainties associated with this value.

To ensure that we have picked a reliable redshift and to mitigate the potential larger uncertainties associated with C IV emission line models (Shen et al. 2011; Chen et al. 2019), we opted to utilize the SDSS data directly and perform modelling on [O III] λ5007. For this purpose, we have used the optical spectrum obtained in 2003 March (MJD 52728) and used two Gaussians to fit [O III] emission line. Our modelling yielded a redshift of 0.0747, a value only 0.00016 larger than the NED estimate. However, this will increase the velocity of the outflow to be $v = -195$ km s^{-1}. Taking all these considerations into account, we utilize the initially assumed redshift throughout this paper, and we assume an uncertainty of $\Delta v \sim 44$ km s^{-1} when needed.

[1]SIMBAD astronomical data base: http://simbad.cds.unistra.fr/simbad/.
[2]NED: https://ned.ipac.caltech.edu/.
[3]SAS: https://dr18.sdss.org/.

3 ANALYSIS

3.1 Ionic column densities

Determining the ionic column densities ($N_{\rm ion}$) of the outflow absorption lines is crucial for understanding the physical properties of the outflow system. While there are two methods to estimate the ionic column densities, we employed the apparent optical depth (AOD) method for all detected absorption lines since all of the identified doublets appear to be saturated (see Section 3.1.1). In this method, the main assumption is that the outflow uniformly and fully covers the source (Spitzer 1968; Savage & Sembach 1991). When using the AOD method, one can infer the column density via the equations (1) and (2) below (Spitzer 1968; Savage & Sembach 1991):

$$I(\lambda) = I_0(\lambda)\, {\rm e}^{-\tau(\lambda)}, \tag{1}$$

in which $I(\lambda)$ and $I_0(\lambda)$ are the intensities with and without the absorption, respectively. $\tau(\lambda)$ is the optical depth of the absorption trough. Then, the ionic column densities can be measured using equation (2) (Arav et al. 2001):

$$N_{\rm ion} = \frac{3.7679 \times 10^{14}}{\lambda_0 f_{\rm ik}} \times \int \tau(v)\, {\rm d}v \ ({\rm cm}^{-2}), \tag{2}$$

where λ_0 is the transition's wavelength and $f_{\rm ik}$ is the oscillator strength of the transition. For more details regarding the AOD method, see Arav et al. (2001), Gabel et al. (2003), and Byun, Arav & Hall (2022c). The other method is called the partial covering (PC) method, and it will not be used in this paper. For a detailed explanation of both methods and to better understand the logic behind them and get a sense of their mathematics, refer to Barlow, Hamann & Sargent (1997), Arav et al. (1999a, b, 2005), de Kool, Korista & Arav (2002), Borguet et al. (2012a), Byun, Arav & Hall (2022b), and Byun et al. (2022c).

Below we explain how various absorption lines were treated and why we applied the AOD method approach in each case. For each absorption line that we were interested in, we used the redshift of the outflow ($z_{\rm outflow}$) to transfer the spectrum from wavelength space to velocity space (refer to Fig. 3). As shown by the dashed lines in Fig. 3, we have chosen a velocity range of −210 to −90 km s^{-1} as our integration range when performing column density calculations. This region was chosen based on the centroid velocity and the absorption trough width of Si IV. Since all the absorption lines result from the same outflow system, we use the same integration range for all.

3.1.1 C IV, Si IV, and N V doublets

The C IV λλ1548, 1551, Si IV λλ1394, 1403, and N V λλ1239, 1243 absorption lines are prominent spectral features observed in AGN outflows. All of these lines are easily detectable in the spectrum of J1429+4518 (see Figs 1 and 2) indicating the presence of an absorption outflow system. However, while these lines are recognized as doublets (and expected to be treated using the PC method), they are all very saturated as their blue-to-red trough ratio is very close

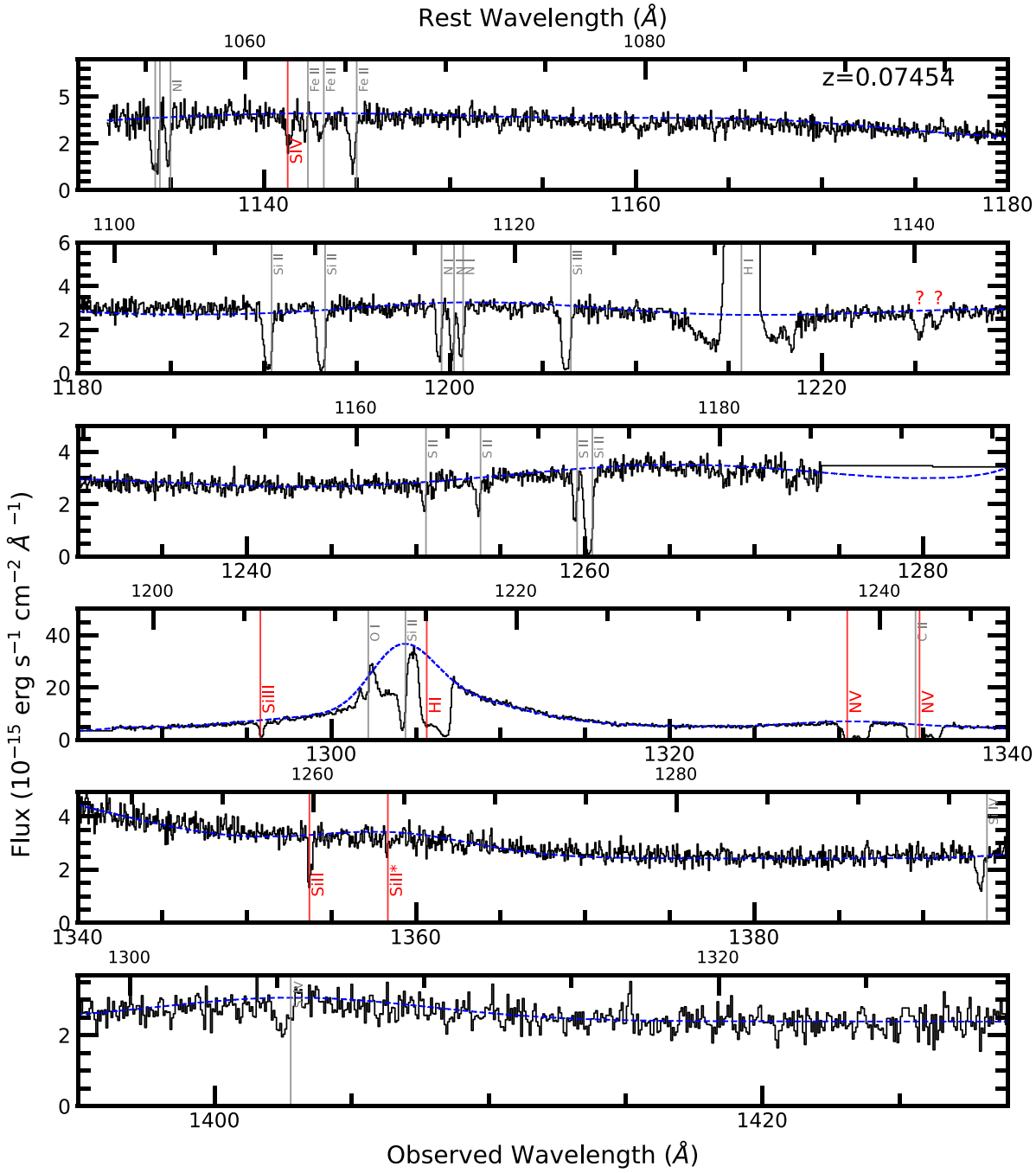

Figure 1. The spectrum of J1429+4518 observed by the *HST*/COS in 2021 September (Putman et al. 2020). The absorption features of the outflow system with a velocity of −151 km s^{-1} are marked with vertical lines and large labels, while the vertical lines wirh small labels show the absorption from the interstellar medium (ISM). The dashed line shows our continuum emission model. The question marks indicate some absorption lines that we could not identify (we confirm they are not C IV resulting from an intervening system).

to 1:1 for all three cases. For this reason, in our calculations, we adopted the AOD results of the red doublet (since it has the lower oscillator strength) and considered them a lower limit to the total ionic column density for each species. Note that for the case of N V, the high-velocity wing of the red doublet is actually Galactic C II λ1334 absorption.

3.1.2 Ly

As shown in Fig. 3, Ly is also suspected of being highly saturated since it has a very large optical depth. For this reason, while we use the AOD method to calculate its ionic column density, we take it as a lower limit and not an accurate measurement.

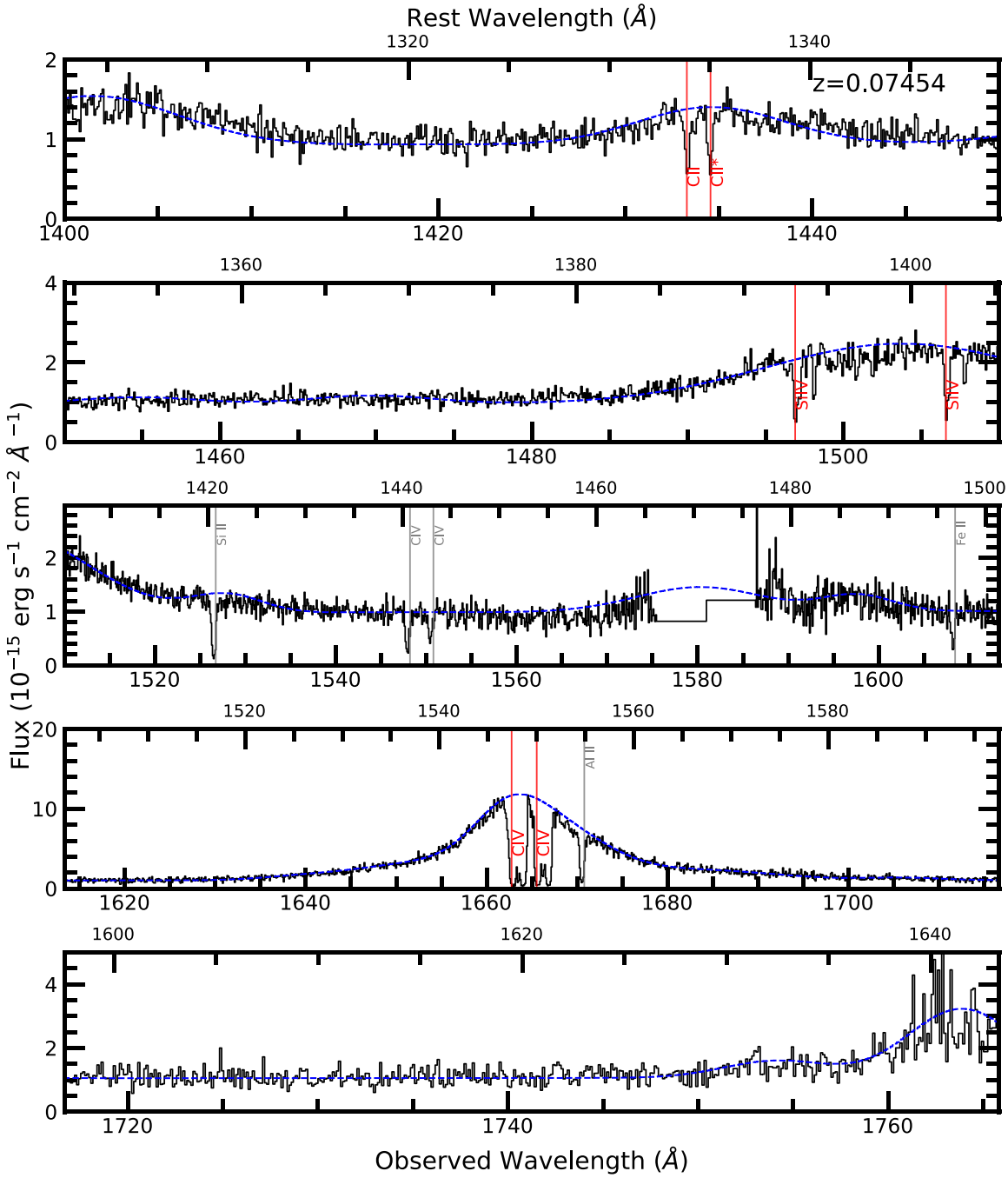

Figure 2. Same as Fig. 1, but the data are from *HST*/COS observations in 2021 December (Putman et al. 2020). Note that since the C IV lines are black at the bottom, the covering fraction of the NAL outflow is estimated to be 1.0.

3.1.3 C II λ1334 and C II λ1336*

Since these two lines are from different energy levels, we employ the AOD method to calculate the column density for each line individually. However, as depicted in Fig. 3, the flux ratio of C II to C II* appears to be approximately 1:1. While it is evident that the lines are not fully saturated (optical depth is not very large), a 1:1 ratio might have resulted from a mild saturation effect. For this reason, we proceed to utilize their column density resulted from the AOD method as a lower limit, not an accurate measurement. In later steps, we use the ratio of $\frac{N_{\rm ion}({\rm C\,II^*})}{N_{\rm ion}({\rm C\,II})}$ to extract a lower limit for the electron number density of the outflow.

3.1.4 Si III λ1206

As marked in Fig. 1, Si III λ1206 is easily identifiable. Since this line is a singlet, we use our usual AOD method to infer its ionic column density. However, since it appears to be very deep (see Fig. 3) and hence probably saturated, we consider the results as a lower limit, not an actual measurement.

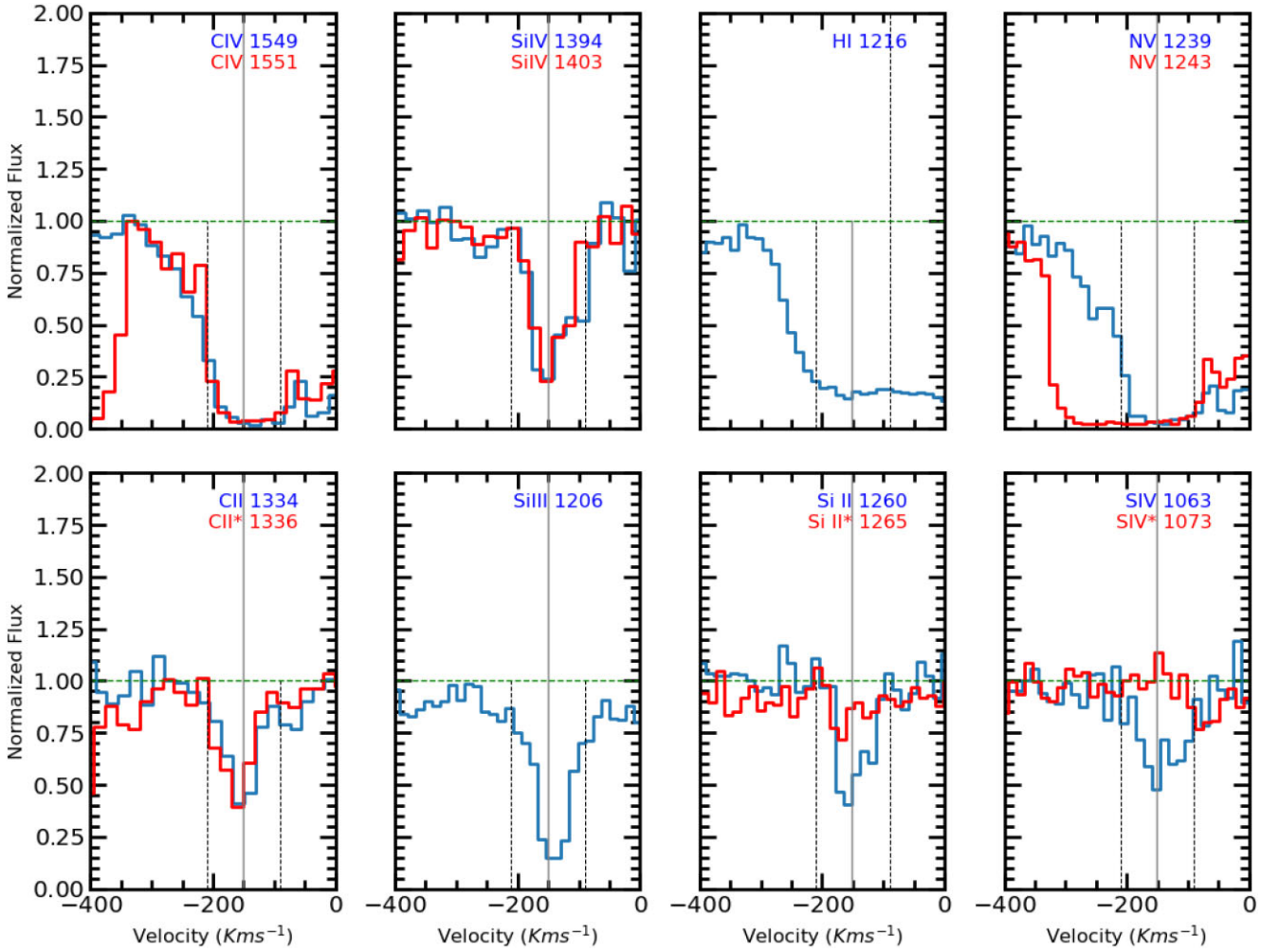

Figure 3. Normalized flux versus velocity for blueshifted absorption lines detected in the spectrum of J1429+4518. The horizontal dashed horizontal line shows the continuum level, and the vertical dashed lines show the region between −210 and −90 km s^{-1}. The vertical solid line indicates the centroid velocity of $v_{\rm centroid} = -151$ km s^{-1}.

3.1.5 Si II λ1260 and Si II λ1265*

Fig. 3 shows that both resonance and excited state absorption lines of Si II ion are detectable. Since the Si II trough is significantly shallower than the Si III trough, we cautiously accept its AOD measurement as a real measurement as opposed to a lower limit. The fact that Si II* is shallower than Si II suggests that we can use their ionic column densities ratio to estimate the electron number density of the outflow (Arav et al. 2018). Later in Section 3.3.1, we discuss this process in more detail.

3.1.6 S IV λ1063 and S IV λ1073*

While we were able to accurately measure the column density of the S IV using the AOD method, S IV* is absent (Fig. 3). For this reason, we used a Gaussian fit based on the S IV absorption line and estimated an upper limit for S IV* ionic column density. Then the ratio of $N_{\rm ion}$(S IV*) to $N_{\rm ion}$(S IV) can be used to extract an upper limit for the electron number density of the outflow system.

Fig. 4 illustrates the Gaussian fit for both the resonance and excited states of the S IV line. It is important to note that we modelled the S IV* state using the best-fitting parameters obtained for the S IV resonance line as the template. The depth of the curve for S IV* was

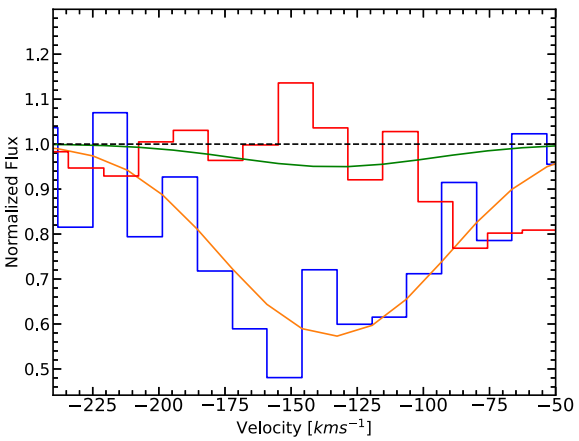

Figure 4. Gaussian modelling (shallow green) of the S IV* λ1073 absorption trough, created by fitting S IV λ1063 line (deep orange) and using its shape as a template, where we have allowed the optical depth to adjust within a 3σ error range. The horizontal dashed line shows the continuum level.

Table 1. The ionic column densities of the absorption lines detected in the J1429+4518 outflow system. Note that the reported/adopted value for C II includes the column densities of C II and C II*. We did not add the systematic error to Si II and Si II* since these two lines are only 5 Å apart and will not be affected much by a systematic error. All of the column density values are in units of 10^{12} cm^{-2}.

Ion	AOD	Adopted
C IV	580^{+50}_{-40}	$>580_{-122}$
Si IV	63^{+7}_{-6}	$>63_{-14}$
Lyα	105^{+2}_{-2}	$>105_{-21}$
N V	503^{+24}_{-31}	$>503_{-103}$
C II	187^{30}_{-27}	$>187_{-46}$
Si II	9^{+1}_{-1}	9^{+1}_{-1}
Si III	18^{+1}_{-1}	$>18_{-4}$
S IV	262^{+31}_{-29}	262^{+61}_{-60}
Si II*	4^{+1}_{-1}	4^{+1}_{-1}

allowed to adjust within a 3σ error range during the fitting process. We have checked the spectrum for any signs of the C III* λ1175 NAL and we were not able to identify any traces of the mentioned line. Table 1 summarizes the results we got from our $N_{\rm ion}$ measurements, along with the numbers we chose to use in the next step, which will assess the outflow characteristics. The adopted errors include the corresponding AOD errors and a systematic error (20 per cent of the adopted value), which are quadratically added together (e.g. Miller et al. 2018, 2020c; Xu et al. 2018).

3.2 Photoionization solution

We calculated the ionic column densities of the mentioned absorption lines for the primary purpose of estimating the characteristics of the outflow, including the total hydrogen column density ($N_{\rm H}$) and the ionization parameter of the system ($U_{\rm H}$; e.g. Xu et al. 2019; Byun, Arav & Walker 2022a; Byun et al. 2022b,c; Walker, Arav & Byun 2022). To do so, we use CLOUDY simulations (Ferland et al. 2017) in which a grid of $N_{\rm H}$ and $U_{\rm H}$ is used to predict the abundance of various ions. Then we constrain the $N_{\rm H}$ and $U_{\rm H}$ values based on our measured ionic column densities. The top panel of Fig. 5 shows the results of this process. To produce this figure, we used the spectral energy distribution (SED) of AGN HE 0238−1904 (hereafter HE 0238; Arav et al. 2013) in CLOUDY and set a large range of grids on $N_{\rm H}$ and $U_{\rm H}$. In Fig. 5 (top panel), the coloured contours show the values labelled 'adopted' in Table 1. As this figure shows, a single-phase solution is sufficient to satisfy the constraints from the ionic column densities. Based on these results, we narrowed down the column density–ionization space to a pair of $N_{\rm H}$ and $U_{\rm H}$ for the absorption outflow system: $U_{\rm H} = -2.0^{+0.1}_{-0.1}$ cm^{-2} and $N_{\rm H} = -19.84^{+0.20}_{-0.20}$ cm^{-2} (reduced $\chi^2 = 2.5$). Note that to produce these results, a solar abundance was assumed.

While the above solution satisfies all the constraints, we examined the dependency of the results on the SED and metallicity. For this purpose, we repeated the same process of prediction $N_{\rm H}$ and $U_{\rm H}$ using another two SEDs, namely the MF87 SED (Mathews & Ferland 1987) and UV-soft SED (Dunn et al. 2010). For all three SEDs, we have also investigated the effects of supersolar metallicity ($Z = 4.68\ Z_\odot$; Ballero et al. 2008; Miller et al. 2020b). The bottom panel of Fig. 5 shows the effects of different SEDs and supersolar metallicity on the results. In this figure, each solid line belongs to the calculations considering a solar metallicity, while dashed lines are

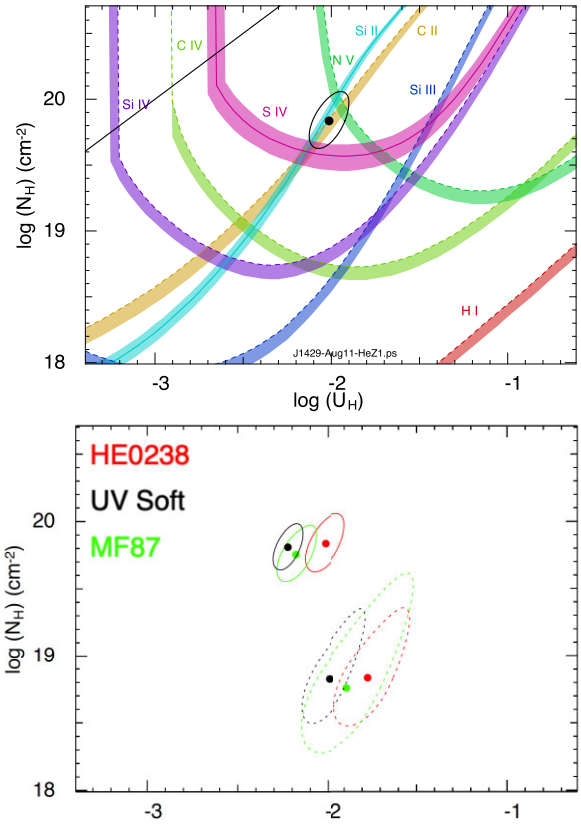

Figure 5. Top panel: Single-phase photoionization solution for the absorption outflow system. Each coloured contour indicates the ionic column densities consistent with the observations (available in Table 1), assuming the HE 0238 SED and solar metallicity. Solid lines within the contours show the ionic column densities taken as measurements, while dashed lines contours belong to lower limits. The shaded bands are the uncertainties added for each contour. The black circle shows the best χ^2 minimization solutions. Bottom panel: The photoionization solution for a total of six models, including three SEDs (HE 0238, MF87, and UV soft) and two metallicities for each: solar metallicity and supersolar metallicity, for a total of six models.

resulted from a supersolar metallicity. These results show that using MF87 and UV-soft SEDs results in a slightly smaller χ^2 (2.3 and 1.5, respectively). However, as discussed by Arav et al. (2013), we prefer to continue using HE 0238 SED since it extends quite far into the extreme UV rest wavelength range.

3.3 Determining the electron number density and the distance of the outflow from the central source

3.3.1 Electron number density

We ran a model of CLOUDY using HE 0238 SED and the $N_{\rm H}$ and $U_{\rm H}$ values to predict the outflow's temperature. This simulation resulted in a temperature of $T \approx 14\,000$ K. Assuming this temperature, we used the CHIANTI 9.0.1 atomic data base (Dere et al. 1997, 2019) to estimate the abundance ratios of excited state to the resonance state for Si II, C II, and S IV as a function of electron number density ($n_{\rm e}$). Fig. 6 illustrates the results. Since Si II's absorptions in both excited and resonance states were reliably measured (Section 3.1.5), we took its ratio as a diagnostics for the electron number density of the outflow (blue curve in Fig. 6). These considerations result in $\log\, n_{\rm e} = 2.75^{+0.20}_{-0.25}$ cm^{-3}. As described in Osterbrock & Ferland (2006) and for a highly ionized plasma, $n_{\rm e} \approx 1.2 n_{\rm H}$, resulting in

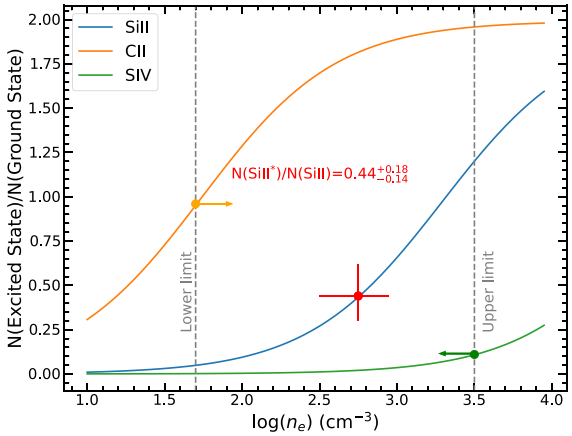

Figure 6. The excited state to resonance state column density ratio versus the electron number density from the CHIANTI atomic data base. We have shown the calculated value from our modelling and marked its corresponding electron number density by a vertical dashed line. Note that these results are sensitive to the temperature, and to produce this plot, we assumed $T = 14\,000$ K.

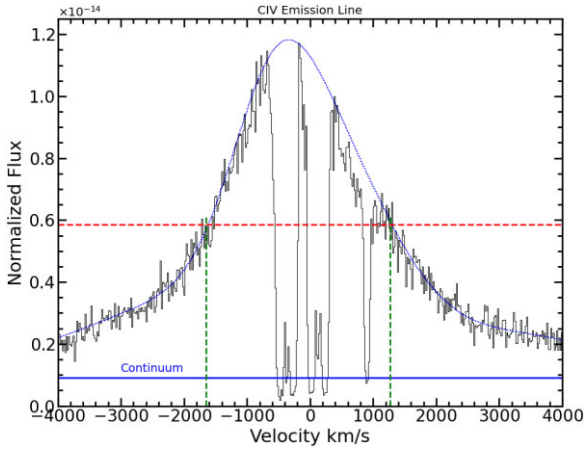

Figure 7. C IV emission line region. The blue line shows our Gaussian fit to the emission spectra. The horizontal dashed line indicates where the half-maximum is, while the vertical dashed lines show the full width at half-maximum (FWHM). The continuum level is shown in the figure, and it is subtracted for the purpose of FWHM determination.

log $n_{\rm H} = 2.67^{+0.20}_{-0.25}$ cm^{-3}. We have also used C II and S IV to predict lower and higher limits for $n_{\rm e}$ (details in Sections 3.1.3 and 3.1.6, respectively). These upper and lower constraints on $n_{\rm e}$ are fully consistent with the Si II*/Si II measurement.

3.3.2 Location of the outflow

Once $N_{\rm H}$, $n_{\rm H}$, and $U_{\rm H}$ are known, we can use equation (14.4) from Osterbrock & Ferland (2006) to extract the location of the outflow:

$$U_{\rm H} \equiv \frac{Q(H)}{4\pi R^2 c\, n_{\rm H}} \Rightarrow R = \sqrt{\frac{Q(H)}{4\pi c\, n_{\rm H} U_{\rm H}}}, \tag{3}$$

where $Q(H)$ (s^{-1}) is the number of hydrogen-ionizing photons emitted by the central object per second, R is the distance between the outflow and the central source, $n_{\rm H}$ is the hydrogen density, and c is the speed of light.

To calculate R, we must first calculate the number of hydrogen-ionizing photons $Q(H)$. To do so, we followed several steps explained below (refer to the works done by Miller et al. 2020a; Byun et al. 2022a,b; Walker et al. 2022).

(i) First, we scaled the SED of HE 0238 to match the continuum flux of J1429+4518 at observed wavelength of $\lambda = 1350$ Å. Based on the *HST* observations we are using in this paper, at the mentioned wavelength $F_\lambda \approx 3 \times 10^{-15}$ erg s^{-1} cm^{-2} Å^{-1}.

(ii) Then, we integrated over the scaled SED for all energies above 1 Ryd (hydrogen ionization potential) to get a value of $1.2^{+0.1}_{-0.1} \times 10^{54}$ s^{-1} for $Q(H)$ and a bolometric luminosity of $L_{\rm bol} = 2.13^{+0.2}_{-0.2} \times 10^{44}$ erg s^{-1}.

(iii) Finally, using these values and equation (3), we predict that the outflow system is located at a distance of $R \approx 275^{+53}_{-46}$ pc from the source.

3.4 Black hole mass and outflow's energetics

3.4.1 Black hole mass and the Eddington luminosity

To get an estimate of the outflow's energetics, including its mass-loss rate and the kinetic luminosity, we need to get a hand on the mass of central black hole (BH) and its Eddington luminosity first.

In 2006, Vestergaard & Peterson (2006) showed that C IV emission line could be used to measure the mass of the BH via this equation

$$\log M_{\rm BH}({\rm C\,IV}) = \log\left(\left[\frac{\rm FWHM(C\,IV)}{1000\,{\rm km\,s^{-1}}}\right]^2 \left[\frac{\lambda L_\lambda(1350\,{\rm Å})}{10^{44}\,{\rm erg\,s^{-1}}}\right]^{0.53}\right). \tag{4}$$

Later in 2017, Coatman et al. (2017) revised equation (4) as below:

$$M_{\rm BH}({\rm C\,IV, Corr.}) = 10^{6.71}\left[\frac{\rm FWHM(C\,IV, Corr.)}{1000\,{\rm km\,s^{-1}}}\right]^2 \times \left[\frac{\lambda L_\lambda(1350\,{\rm Å})}{10^{44}\,{\rm erg\,s^{-1}}}\right]^{0.53}, \tag{5}$$

where

$${\rm FWHM(C\,IV, Corr.)} = \frac{\rm FWHM(C\,IV, Meas.)}{(0.41 \pm 0.02)\frac{\rm C\,IV\ blueshift}{1000\,{\rm km\,s^{-1}}} + (0.62 \pm 0.04)}. \tag{6}$$

As shown in Fig. 2, we can easily identify the C IV emission and use its full width at half-maximum (FWHM) to achieve the mass of the BH. Fig. 7 shows our Gaussian model to fit the spectra at C IV region, in which we have modelled the C IV emission with a single Gaussian. Based on this figure, the FWHM is measured to be ≈3100 km s^{-1} for the C IV emission line. We also measured an average flux of 1×10^{-15} erg s^{-1} cm^{-2} Å^{-1} for $\lambda_{\rm rest} = 1350$ Å, which for our narrow outflow system results in $\lambda L_\lambda = 1.16 \times 10^{42}$ erg s^{-1}. Using these values in the equations (6) and (5), we get a BH mass of $M_{\rm BH} = 7.5 \times 10^6$ M$_\odot$, resulting in an Eddington luminosity of $L_{\rm Edd} = 8.8 \times 10^{44}$ erg s^{-1}.

3.4.2 Outflow's energetics

Using outflow's R and $N_{\rm H}$ obtained above, we can estimate the mass-loss rate and the kinetic luminosity of the outflow using the following equations (Borguet et al. 2012b):

$$\dot{M} \simeq 4\pi\Omega R N_{\rm H} \mu m_{\rm p} v, \tag{7}$$

$$\dot{E}_{\rm K} \simeq \frac{1}{2}\dot{M} v^2. \tag{8}$$

Table 2. Physical properties of the narrow absorption line (NAL) outflow system.

$\log N_{\rm H}$ (cm^{-2})	$19.84^{+0.20}_{-0.20}$
$\log U_{\rm H}$ (dex)	$-2.0^{+0.1}_{-0.1}$
$\log n_{\rm e}$ (cm^{-3})	$2.75^{+0.20}_{-0.20}$
R (pc)	275^{+53}_{-46}
$\dot{M}$ (M$_\odot$ yr^{-1})	$0.22^{+0.09}_{-0.06}$
$\log \dot{E_K}$ (erg s^{-1})	$39.3^{+0.1}_{-0.2}$
$\dot{E_{\rm K}}/L_{\rm Edd}$	$2.0^{+0.9}_{-0.7} \times 10^{-6}$
$\dot{E_{\rm K}}/L_{\rm Bol}$	$8.5^{+3.0}_{-2.0} \times 10^{-6}$

In equation (7), $\mu = 1.4$ is the mean atomic mass per proton, v is the velocity of the outflow, and $m_{\rm p}$ is the mass of a proton (Borguet et al. 2012a). In the mentioned equation, Ω is the global covering factor defined as the percentage of the source covered by the outflow in all directions (not only line of sight). We assume $\Omega = 0.5$ as Misawa et al. (2007b) explain that intrinsic NALs are observed in at least 50 per cent of AGNs. In an earlier study published in 2003, Vestergaard (2003) discusses more than half of the AGNs embed NALs. All these studies are in agreement with the 50–70 per cent population ratio of NALs among Seyfert 1 galaxies as reported by Crenshaw et al. (1999). Assuming all these values and solving equations (7) and (8) for the mass-loss rate and the kinetic luminosity results in $\dot{M} = 0.22^{+0.09}_{-0.06}$ M$_\odot$ yr^{-1} and $\log \dot{E_{\rm K}} = 39.3^{+0.1}_{-0.2}$ erg s^{-1}. Table 2 summarizes all these results along with the results from Section 3.

As reported in Table 2, the ratio of outflow system's kinetic luminosity to the source's Eddington luminosity is ≈0.0002 per cent. Hopkins & Elvis (2010) explain that an outflow system must have an $\dot{E_{\rm K}}/L_{\rm Edd}$ of at least ≈0.5 per cent to contribute to the AGN outflow, verifying that the NAL outflow system identified here does not contribute to AGN feedback processes.

It is worth mentioning that if we take the redshift considerations into account (Section 2.1) and assume that the outflow has a velocity of approximately −195 km s^{-1}, then $\dot{M} = 0.27$ M$_\odot$ yr^{-1} and $\log \dot{E_{\rm K}} = 39.5$ erg s^{-1}. Based on these values, the ratio of outflow system's kinetic luminosity to the source's Eddington luminosity would be ≈0.0004 per cent. This indicates that for the [O III]-based redshift, the above discussion remains valid, and this outflow contributes minimally or not at all to the AGN feedback process.

4 DISCUSSION

4.1 The thermal stability curve

When gas is photoionized, it will reach the equilibrium defined by an ionization parameter (Tarter, Tucker & Salpeter 1969; Kallman & Bautista 2001),

$$\xi \equiv \frac{L_{\rm ion}}{n_{\rm H} r^2}\ ({\rm erg\,cm\,s^{-1}}), \tag{9}$$

and a specific temperature. This equilibrium arises due to the interplay between various heating and cooling mechanisms that depend on the gas's physical and chemical attributes and the characteristics of the intrinsic radiation of the source.

It is common to represent these balanced states on a stability curve, depicted in a diagram with temperature (T) on the vertical axis and the ratio of ξ/T on the horizontal axis (e.g. Krolik, McKee & Tarter 1981). When we assume that $L/n(H)r^2$ remains constant, the latter parameter, $\xi/T \propto p_{\rm rad}/p_{\rm gas}$, indicates the gas pressure. The thermal stability curve (S-curve) for J1429+4518 is produced using CLOUDY and is shown in Fig. 8. To create the stability curve, we have used the previously mentioned HE 0238 SED and the outflow's characteristics are adopted from Table 2. In this figure, the region on the left-hand side of the curve is dominated by cooling processes, while heating processes dominate the right-hand side. A positive slope on the S-curve happens when an increase in T (due to an isobaric perturbation) will move the gas to the cooling region and so revert the gas to the same equilibrium state. Such equilibrium states are considered to be thermally stable. The green circle in Fig. 8 indicates where our NAL outflow is located regarding the stability. Based on this plot, the outflow is on the positive slope and hence it is assumed to be thermally stable.

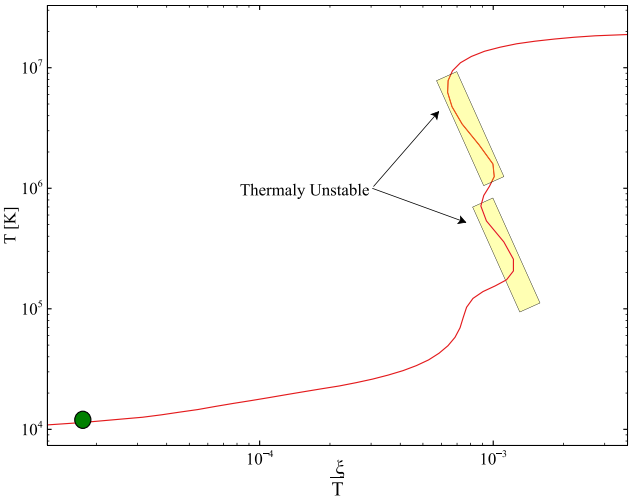

Figure 8. The photoionization stability curve (S-curve) for J1429+4518. The green circle indicates the narrow absorption outflow system discussed in this paper. The rectangles indicate the negative-slope regions, meaning any gas with those characteristics would be unstable.

4.2 The importance of the NALs

Hamann et al. (2011) explain that to understand AGN outflows better, we need clearer information about the different types of outflows, including NAL outflows. For a while now, there has been an ongoing discussion about whether the NALs and BALs have any connection or relationship (Weymann et al. 1979). Furthermore, there is an ongoing debate about how these associated NALs and BALs might fit into the overall development or evolution of AGNs (Briggs, Turnshek & Wolfe 1984; Hamann et al. 2001).

It is not straightforward to detect NAL outflows because they are hard to identify: most narrow lines we see in AGN spectra come from unrelated cosmic gas, not from the AGN themselves. However, some studies suggest that a significant part of these NALs actually come from AGN outflows (e.g. Richards 2001; Nestor, Hamann & Rodriguez Hidalgo 2008; Wild et al. 2008).

4.3 Similarity to Milky Way outflows

The NAL outflow system in J1429+4518 shows some remarkable similarity to the two bipolar lobe outflows observed in the Milky Way

by *XMM–Newton* and *Chandra* (see Ponti et al. 2019, fig. 1). One of these lobe outflows extends up to 160 pc from the Galactic Centre in the northern direction. The second lobe, situated to the south, extends even further, reaching beyond the southern *Fermi* bubble's base and spanning approximately 250 pc (Veilleux et al. 2020). Notably, the distances from their central source align closely with the 275 pc measured for our study's NAL outflow system. Furthermore, their kinematic luminosities are estimated at $\log \dot{E}_{\rm K} = 39.6$ erg s^{-1} (Ponti et al. 2019) – merely 0.3 dex larger than that of our outflow system – these similarities are striking. Finally, the comparability of the Milky Way's BH mass ($M_{\rm BH} = 4.15 \times 10^6$ M$_\odot$; GRAVITY Collaboration 2019) with that of J1429+4518 ($M_{\rm BH} = 6.7 \times 10^6$ M$_\odot$) along with the mentioned similarities in the outflow's measurements suggests a common origin for the two outflows. It is worth noting that other outflows in the Milky Way are located farther away or have much larger kinetic luminosity (Veilleux et al. 2020).

5 CONCLUSIONS

In this paper, we analysed two data sets from *HST*/COS 2021 observations of Seyfert 1 galaxy J1429+4518. We successfully identified an NAL outflow system located ∼275 pc away from the central source. This outflow was identified through narrow absorption troughs of C IV, Si IV, N IV, Lyα, C II, C II*, Si II, Si II*, Si III, and S IV. We measured the centroid velocity of the outflow system to be −151 km s^{-1} and extracted the ionic column densities of the absorption lines using the AOD method.

As the next step, measured ionic column densities were used to determine the total hydrogen column density ($\log N_{\rm H} = 19.84$ erg s^{-1}) and the ionization state ($\log U_{\rm H} = -2.0$) of the NAL outflow. This was done by using χ^2-minimization solutions and performing CLOUDY simulations. We also used the ratio of the ionic column densities of Si II* to Si II for measuring the electron number density ($\log n_{\rm e} = 2.75$ cm^{-3}) and hence its hydrogen density. Having the hydrogen density enabled us to estimate the outflow location mentioned above. We followed all these calculations by estimating the energetics of the outflow: this outflow has a kinetic luminosity of $\log \dot{E}_{\rm K} = 39.3$ erg s^{-1} and its mass-loss rate is measured to be $\dot{M} = 0.22$ M$_\odot$ yr^{-1}.

The NAL outflow of J1429+4518 is thermally stable, but it does not contribute to AGN feedback processes since its kinetic luminosity is only ≈0.00025 per cent of the Eddington luminosity of the central source. Finally, we note that this NAL outflow exhibits a striking similarity to the two bipolar lobe outflows detected in the Milky Way through observations conducted by *XMM–Newton* and *Chandra*. The similarities in their energetics and location, and having central BHs with similar masses, strongly suggest that these outflows might have a common origin.

ACKNOWLEDGEMENTS

We express our appreciation to the anonymous reviewer whose feedback has contributed to the enhancement of this paper. We acknowledge support from NSF grant AST 2106249, as well as NASA STScI grants AR-15786, AR-16600, AR-16601, and HST-AR-17556.

DATA AVAILABILITY

The data of J1429+4518 described in this paper may be obtained from the *MAST* archive at https://dx.doi.org/10.17909/mzeb-fm44.

REFERENCES

Arav N., Korista K. T., de Kool M., Junkkarinen V. T., Begelman M. C., 1999a, ApJ, 516, 27
Arav N., Becker R. H., Laurent-Muehleisen S. A., Gregg M. D., White R. L., Brotherton M. S., de Kool M., 1999b, ApJ, 524, 566
Arav N., Brotherton M. S., Becker R. H., Gregg M. D., White R. L., Price T., Hack W., 2001, ApJ, 546, 140
Arav N., Kaastra J., Kriss G. A., Korista K. T., Gabel J., Proga D., 2005, ApJ, 620, 665
Arav N., Borguet B., Chamberlain C., Edmonds D., Danforth C., 2013, MNRAS, 436, 3286
Arav N., Liu G., Xu X., Stidham J., Benn C., Chamberlain C., 2018, ApJ, 857, 60
Astropy Collaboration, 2013, A&A, 558, A33
Astropy Collaboration, 2018, AJ, 156, 123
Ballero S. K., Matteucci F., Ciotti L., Calura F., Padovani P., 2008, A&A, 478, 335
Barlow T. A., Hamann F., Sargent W. L. W., 1997, in Aravm N., Shlosman I., Weymann R. J., eds, ASP Conf. Ser. Vol. 128, Mass Ejection from Active Galactic Nuclei. Astron. Soc. Pac., San Francisco, p. 13
Bennett C. L., Larson D., Weiland J. L., Hinshaw G., 2014, ApJ, 794, 135
Borguet B. C. J., Edmonds D., Arav N., Dunn J., Kriss G. A., 2012a, ApJ, 751, 107
Borguet B. C. J., Edmonds D., Arav N., Benn C., Chamberlain C., 2012b, ApJ, 758, 69
Briggs F. H., Turnshek D. A., Wolfe A. M., 1984, ApJ, 287, 549
Byun D., Arav N., Walker A., 2022a, MNRAS, 516, 100
Byun D., Arav N., Hall P. B., 2022b, MNRAS, 517, 1048
Byun D., Arav N., Hall P. B., 2022c, ApJ, 927, 176
Chen Z.-F., Pan D.-S., 2017, ApJ, 848, 79
Chen Z.-F., Qin Y.-P., 2013, ApJ, 777, 56
Chen Z.-F., Huang W.-R., Pang T.-T., Huang H.-Y., Pan D.-S., Yao M., Nong W.-J., Lu M.-M., 2018a, ApJS, 235, 11
Chen Z.-F., Pang T.-T., He B., Huang Y., 2018b, ApJS, 236, 39
Chen Z.-F., Yi S.-X., Pang T.-T., Chen Z.-G., Gui R.-J., Wang Z.-W., Mo X.-H., Yi T.-F., 2019, ApJS, 244, 36
Chen Z.-F., Qin H.-C., Gui R.-J., Yi S.-X., Chen Z.-G., Gao Y.-C., Pang T.-T., Mo X.-H., 2020, ApJS, 250, 3
Chen Z., He Z., Ho L. C., Gu Q., Wang T., Zhuang M., Liu G., Wang Z., 2022, Nat. Astron., 6, 339
Coatman L., Hewett P. C., Banerji M., Richards G. T., Hennawi J. F., Prochaska J. X., 2017, MNRAS, 465, 2120
Crenshaw D. M., Kraemer S. B., Boggess A., Maran S. P., Mushotzky R. F., Wu C.-C., 1999, ApJ, 516, 750
de Kool M., Korista K. T., Arav N., 2002, ApJ, 580, 54
Dere K. P., Landi E., Mason H. E., Monsignori Fossi B. C., Young P. R., 1997, A&AS, 125, 149
Dere K. P., Del Zanna G., Young P. R., Landi E., Sutherland R. S., 2019, ApJS, 241, 22
Dunn J. P. et al., 2010, ApJ, 709, 611
Ferland G. J. et al., 2017, Rev. Mex. Astron. Astrofis., 53, 385
Gabel J. R. et al., 2003, ApJ, 583, 178
GRAVITY Collaboration, 2019, A&A, 625, L10
Hamann F. W., Barlow T. A., Chaffee F. C., Foltz C. B., Weymann R. J., 2001, ApJ, 550, 142
Hamann F., Kanekar N., Prochaska J. X., Murphy M. T., Ellison S., Malec A. L., Milutinovic N., Ubachs W., 2011, MNRAS, 410, 1957
Harris C. R. et al., 2020, Nature, 585, 357
He Z. et al., 2022, Sci. Adv., 8, eabk3291
Hopkins P. F., Elvis M., 2010, MNRAS, 401, 7
Hunter J. D., 2007, Comput. Sci. Eng., 9, 90
Itoh D., Misawa T., Horiuchi T., Aoki K., 2020, MNRAS, 499, 3094
Kallman T., Bautista M., 2001, ApJS, 133, 221
Krolik J. H., McKee C. F., Tarter C. B., 1981, ApJ, 249, 422
Mathews W. G., Ferland G. J., 1987, ApJ, 323, 456

Miller T. R., Arav N., Xu X., Kriss G. A., Plesha R. J., Benn C., Liu G., 2018, ApJ, 865, 90
Miller T. R., Arav N., Xu X., Kriss G. A., Plesha R. J., 2020a, ApJS, 247, 39
Miller T. R., Arav N., Xu X., Kriss G. A., Plesha R. J., 2020b, ApJS, 247, 41
Miller T. R., Arav N., Xu X., Kriss G. A., Plesha R. J., 2020c, ApJS, 249, 15
Misawa T., Charlton J. C., Eracleous M., Ganguly R., Tytler D., Kirkman D., Suzuki N., Lubin D., 2007a, ApJS, 171, 1
Misawa T., Eracleous M., Charlton J. C., Ganguly R., Tytler D., Kirkman D., Suzuki N., Lubin D., 2007b, in Ho L. C., Wang J.-M., eds, ASP Conf. Ser. Vol. 373, The Central Engine of Active Galactic Nuclei. Astron. Soc. Pac., San Francisco, p. 291
Nestor D., Hamann F., Rodriguez Hidalgo P., 2008, MNRAS, 386, 2055
Osterbrock D. E., Ferland G. J., 2006, Astrophysics of Gaseous Nebulae and Active Galactic Nuclei, 2nd edn. University Science Books, Sausalito, CA
Ponti G. et al., 2019, Nature, 567, 347
Putman M. E., Burchett J. N., Emerick A., Kirby E., McQuinn K. B. W., Oppenheimer B. D., Werk J. K., Zheng Y., 2020, HST Proposal, Cycle 28, ID #16301
Reback J. et al., 2021, pandas-dev/pandas: Pandas 1.3.5 (v1.3.5). Zenodo (https://doi.org/10.5281/zenodo.5774815)
Richards G. T., 2001, ApJS, 133, 53
Savage B. D., Sembach K. R., 1991, ApJ, 379, 245
Scannapieco E., Oh S. P., 2004, ApJ, 608, 62
Shen Y., Ménard B., 2012, ApJ, 748, 131
Shen Y. et al., 2011, ApJS, 194, 45
Silk J., Rees M. J., 1998, A&A, 331, L1
Spitzer L., 1968, Diffuse Matter in Space. Interscience Publication, New York
Tarter C. B., Tucker W. H., Salpeter E. E., 1969, ApJ, 156, 943
Vayner A. et al., 2021, ApJ, 919, 122
Veilleux S., Maiolino R., Bolatto A. D., Aalto S., 2020, A&AR, 28, 2
Vestergaard M., 2003, ApJ, 599, 116
Vestergaard M., Peterson B. M., 2006, ApJ, 641, 689
Virtanen P. et al., 2020, Nat. Methods, 17, 261
Walker A., Arav N., Byun D., 2022, MNRAS, 516, 3778
Weymann R. J., Williams R. E., Peterson B. M., Turnshek D. A., 1979, ApJ, 234, 33
Wild V. et al., 2008, MNRAS, 388, 227
Xu X., Arav N., Miller T., Benn C., 2018, ApJ, 858, 39
Xu X., Arav N., Miller T., Benn C., 2019, ApJ, 876, 105
Yuan F., Yoon D., Li Y.-P., Gan Z.-M., Ho L. C., Guo F., 2018, ApJ, 857, 121

This paper has been typeset from a TEX/LATEX file prepared by the author.